The Astrophysical Journal Letters, 955:L14 (13pp), 2023 September 20 https://doi.org/10.3847/2041-8213/acf76b

Dynamical Evolution of White Dwarfs in Triples in the Era of Gaia

Cheyanne Shariat[1,2], Smadar Naoz[1,2], Bradley M. S. Hansen[1,2], Isabel Angelo[1,2], Erez Michaely[1,2], and Alexander P. Stephan[3,4]
[1] Department of Physics and Astronomy, University of California, Los Angeles, Los Angeles, CA 90095, USA; cheyanneshariat@ucla.edu
[2] Mani L. Bhaumik Institute for Theoretical Physics, University of California, Los Angeles, Los Angeles, CA 90095, USA
[3] Department of Astronomy, The Ohio State University, 4055 McPherson Laboratory, Columbus, OH 43210, USA
[4] Center for Cosmology and AstroParticle Physics, The Ohio State University, Columbus, OH 43210, USA
Received 2023 June 28; revised 2023 August 28; accepted 2023 September 6; published 2023 September 20

Abstract

The Gaia mission has detected many white dwarfs (WDs) in binary and triple configurations, and while observations suggest that triple-stellar systems are common in our Galaxy, not much attention was devoted to WDs in triples. For stability reasons, these triples must have hierarchical configurations, i.e., two stars are on a tight orbit (the inner binary), with the third companion on a wider orbit about the inner binary. In such a system, the two orbits torque each other via the eccentric Kozai–Lidov mechanism, which can alter the orbital configuration of the inner binary. We simulate thousands of triple-stellar systems for over 10 Gyr, tracking gravitational interactions, tides, general relativity, and stellar evolution up to their WD fate. As demonstrated here, three-body dynamics coupled with stellar evolution is a critical channel to form tight WD binaries or merge a WD binary. Among these triples, we explore their manifestations as cataclysmic variables, Type Ia supernovae, and gravitational-wave events. The simulated systems are then compared to a sample of WD triples selected from the Gaia catalog. We find that including the effect of mass-loss-induced kicks is crucial for producing a distribution of the inner binary–tertiary separations that is consistent with Gaia observations. Lastly, we leverage this consistency to estimate that, at minimum, 30% of solar-type stars in the local 200 pc were born in triples.

Unified Astronomy Thesaurus concepts: Astrodynamics (76); Three-body problem (1695); Stellar evolution (1599); Theoretical models (2107); White dwarf stars (1799); Binary stars (154); Common envelope evolution (2154); Trinary stars (1714); Gravitational wave sources (677); Cataclysmic variable stars (203)

1. Introduction

The European Space Agency's Gaia mission (Gaia Collaboration et al. 2016) is instrumental in understanding the properties, kinematics, and dynamics of white dwarfs (WDs). To date, Gaia has identified >350,000 WDs (e.g., Jiménez-Esteban et al. 2018; Gentile Fusillo et al. 2019, 2021), allowing for an unprecedented opportunity to test our theoretical understanding of the dynamical evolution of WDs and their companions. Gaia's precise measurements of WDs have already led to an abundance of novel insights into WD binary evolution (e.g., El-Badry & Rix 2018; El-Badry et al. 2018; Cheng et al. 2020; Ren et al. 2020; Torres et al. 2022) and the physical properties (i.e., age, composition, cooling function, etc.) of local WDs (e.g., Cheng et al. 2019; Blouin et al. 2020; Chandra et al. 2020; Tremblay et al. 2020; Zorotovic & Schreiber 2020, 2022; Blouin & Daligault 2021; Torres et al. 2021; Blouin 2022). However, the population of observed WD triples from Gaia has received little attention. We aim to leverage this data from the recent Gaia Data Release 3 to test our understanding of the complex dynamical evolution of triple-stellar systems.

Most stars end their lives as WDs. Interestingly, between 25% and 40% of these WDs reside in a binary or multiple star system (e.g., Raghavan et al. 2010; Holberg et al. 2016; Hollands et al. 2018, the latter studies focused on the local 25 pc). The multiplicity fraction of WDs is not surprising, given that nearly half of all Sun-like stars are observed to be in binary, or higher-order configurations (e.g., Duquennoy & Mayor 1991; Tokovinin 1997; Raghavan et al. 2010). In fact, it has recently been suggested that 21%–36% of wide double WD binaries were once a triple (Heintz et al. 2022). Furthermore, observations suggest that 40% of older stars have companions (such as WDs), and most (⩾70%) A and B spectral type stars have one or more companions (e.g., Raghavan et al. 2010; Moe & Di Stefano 2017).

The WDs in triples and higher-order systems are essential to understanding a variety of binary exotica. For example, stellar triples and binaries containing at least one WD are key progenitors for Type Ia supernovae (e.g., Parthasarathy et al. 2007; Thompson 2011; Katz & Dong 2012; Hamers et al. 2013, 2018; Toonen et al. 2018; Michaely 2021; Michaely & Shara 2021; Liu et al. 2023; see Wang & Han 2012, for a review on SNe Ia) post-common envelope binaries (e.g., Toonen & Nelemans 2013; Zorotovic et al. 2014; Hernandez et al. 2022), and cataclysmic variables (e.g., Nelemans et al. 2001; Knigge et al. 2011; Pala et al. 2017). Furthermore, double WD binaries are the most numerous sources of gravitational-wave (GW) emission, making them primary targets for the prospective Laser Interferometer Space Antenna (LISA; e.g., Amaro-Seoane et al. 2017; Wang et al. 2021; Xuan et al. 2021; Seto 2022). LISA detections of double WDs will provide key insights toward understanding the binary evolution of WDs (e.g., Korol et al. 2018) and will allow better constraints on the structure of our Galaxy (e.g., Breivik et al. 2020b) and the galactic center (e.g., Wang et al. 2021; Xuan et al. 2023).

The WDs embedded in triple systems explore a broader range of dynamical behavior that cannot be observed in binary systems alone. In general, for stability reasons, triple star systems have a hierarchical configuration—two of the stars are in a close binary orbit while the third companion is farther away.[5] In hierarchical triples, an interesting dynamical phenomenon is introduced: the eccentric Kozai–Lidov mechanism (EKL; Kozai 1962; Lidov 1962; see Naoz 2016, for a review).

The EKL-induced effects from a faraway companion star can cause eccentricity and inclination oscillations to the inner binary, which lead to complex dynamical changes to the evolution of the system. High eccentricities caused by EKL, for example, can lead the inner binary to tighten or even merge (e.g., Naoz 2016). This has been noted to be of special significance in double WD (DWD) binaries, potentially explaining an accelerated rate of observed supernovae (e.g., Thompson 2011), though the efficiency of this merger channel remains unclear (Hamers et al. 2013, 2018; Prodan et al. 2013; Toonen et al. 2018).

Notably, post-main-sequence stellar evolution can have a significant effect on the dynamical evolution of binaries and triples (e.g., Perets & Kratter 2012; Shappee & Thompson 2013; Naoz 2016; Stephan et al. 2016, 2017, 2018, 2019, 2021; Petrovich & Muñoz 2017; Toonen et al. 2020, 2022; Angelo et al. 2022; Hamers et al. 2022; Stegmann et al. 2022; Kummer et al. 2023).

In this work, we provide a comprehensive investigation of the long-term (>10 Gyr) dynamical evolution of stellar triples as one or more of their components evolve into WDs. We then assess the various outcomes, properties, and signatures of end states that contain WDs. The detailed triple-evolution code includes EKL, general relativity (GR), tides, and post-main-sequence evolution, thus allowing us to provide a robust comparison to Gaia's observed WD population.

The paper is organized as follows: in Section 2, we describe our numerical setup and methodology for the simulations and observations. Section 3 is where we outline and analyze the results of our dynamical simulations. In Section 4, we compare our results to Gaia, taking into account both internal and external perturbations attributed to various physical effects. Lastly, we discuss our results and provide the major conclusions in Section 5. Any supplementary equations and figures are provided in the Appendices (Appendices A–D).

2. Methodology

2.1. Physical Processes and Numerical Setup

Consider a hierarchical triple system of masses m_1, m_2 on a tight inner orbit, and m_3 on a wider orbit. This system has an inner (outer) semimajor axis a_1 (a_2), eccentricity e_1 (e_2), argument of periapsis ω_1 (ω_2), and inclinations with respect to the total angular momentum i_1 (i_2). Here we use the invariable plane for reference, where the z-axis is parallel to the total angular momentum (see Naoz 2016, for a full set of equations and definitions).

We solve the equations of motion of the hierarchical triple-body system up to the octupole level of approximation; see Naoz (2016) for the full set of equations. We also include general relativistic precession up to the first post-Newtonian approximation for the inner and outer orbit (e.g., Naoz et al. 2013b). For the mass ratio and scales studied here, these precessions are a sufficient description of the dynamics (e.g., Naoz et al. 2013b; Lim & Rodriguez 2020; Kuntz 2022).

We adopt the equilibrium tides model for both inner binary members, following Hut (1980), Eggleton et al. (1998), and Kiseleva et al. (1998). This model includes rotational precession, tidal precession, and tidal dissipation (modeled as fixed viscous times of 5 yr for each star, following Naoz & Fabrycky 2014). Using this tidal description, we can follow the precession of the spin of each star in the inner binary due to the stars' oblateness and tidal torques (e.g., Naoz & Fabrycky 2014). We use different tidal models for (radiative) main-sequence (MS) and (convective) red giant stars (e.g., Zahn 1977). The switch between tidal models is taking place as a function of stellar type and mass (see Stephan et al. 2018, 2019, 2021; Rose et al. 2019). Note that during the WD stage, equilibrium tides are assumed.

Stellar evolution plays an important role in the evolution of triples (e.g., Naoz 2016; Toonen et al. 2016, 2020, 2022). Specifically, the mass loss associated with the Asymptotic Giant Branch phase can retrigger the EKL mechanism by changing the mass ratio or by expanding the inner orbit's semimajor axis faster than that of the outer binary (Perets & Kratter 2012; Shappee & Thompson 2013; Michaely & Perets 2014; Naoz 2016; Stephan et al. 2016, 2017). We thus follow the post-mainsequence evolution of stars using the Single Stellar Evolution (SSE) code (Hurley et al. 2000). See Naoz (2016), Stephan et al. (2016, 2017, 2018, 2019, 2021) and Angelo et al. (2022) for a detailed description of the triple with stellar evolution code.

The simulations are run for an upper limit of 12.5 Gyr but are stopped earlier if the inner binary either (1) crosses the Roche limit or (2) becomes tidally locked. The first condition checks explicitly if the binary is tidally locked. For the first condition, we define the Roche limit of a star with mass m_j, with radius r_j in a binary as (e.g., Paczyński 1971; Eggleton 1983):

$$R_{\mathrm{Roche},j} \sim 1.66 \times r_j \left(\frac{m_j}{m_1 + m_2}\right)^{-1/3}, \quad (1)$$

where $j = 1, 2$ for the two components of the inner binary. In the second condition, we consider an inner binary to be tidally locked if $e_1 < 0.001$ and either $a_1 < 0.1$ au or $a_1 \leqslant 4R_{\mathrm{Roche}}$.

When the inner binary fulfills either one of these stopping conditions, we follow its evolution using COSMIC Breivik et al. (2020a) binary stellar evolution code (a procedure similar to Stephan et al. 2019; Wang et al. 2021). The COSMIC models the stellar evolution coupled with mass transfer and common envelope and tidal evolution. We keep the default parameters for the code, where the common envelope efficiency is set constant as $\alpha = 1.0$. See Breivik et al. (2020a) for an outline of the other default parameters and their values.

The mass loss during the binary stellar evolution portion is modeled as being either adiabatic (slow and isotropic) or impulsive for the tertiary. The adiabatic approximation is used when the mass loss of the inner binary during one outer orbit, is much smaller than the total mass of the system. At that time, we assume that the inner orbit is decoupled from EKL and can only undergo EKL evolution after the binary interaction ends.

[5] We note that our limitation to a hierarchical configuration is rather conservative. It was shown that deviation from the hierarchy can lead to even higher eccentricity excitations rather than immediate instability (Grishin et al. 2018; Bhaskar et al. 2020; Mushkin & Katz 2020; Zhang et al. 2023).

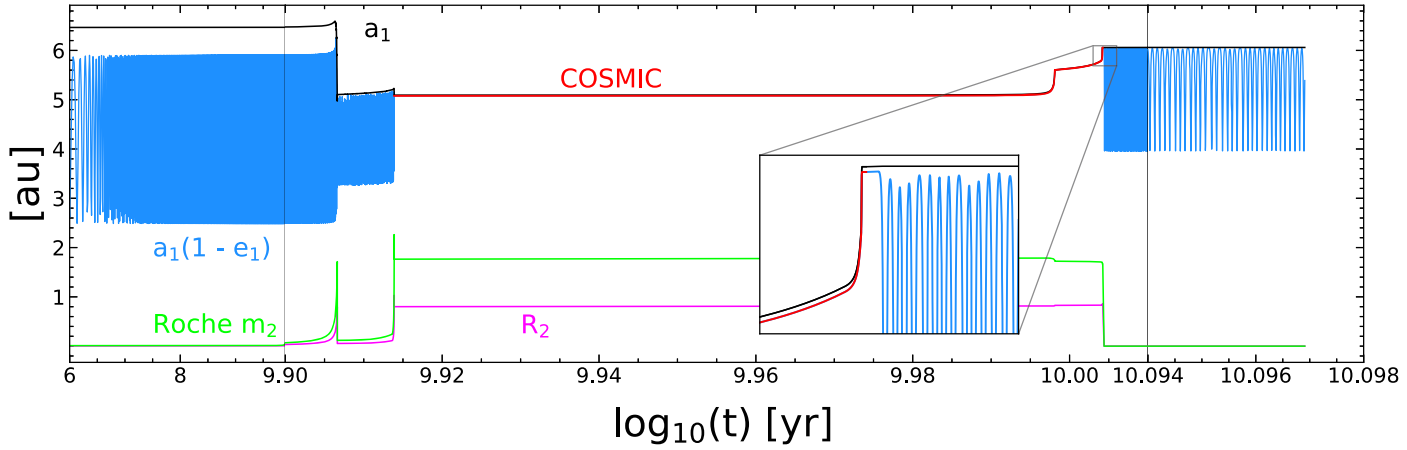

Figure 1. Time-evolution of the semimajor axis and periastron of the inner binary in a representative triple system. After the 12.5 Gyr, the system became a double WD inner binary orbited by a low-mass main-sequence companion. The oscillating blue line represents the evolution in the triple code, and the red line (labeled COSMIC) shows the binary evolution in COSMIC. As one of the stars in the inner binary evolved into a Giant at 8.2 Gyr ($10^{9.91}$ yr), the binary became tidally locked because $e_1 < 0.01$ and $a_1 \leqslant 4\mathrm{Roche}_2$. We then evolved this binary using COSMIC for 1.9 Gyr, until the star evolved into a WD, creating a WDMS binary that is no longer tidally locked. After updating the tertiary star's orbital parameters, we then inserted this triple back into the triple-evolution code to finish its evolution until 12.5 Gyr. Initially, this system had $m_1 = 1.09\ M_\odot$, $m_2 = 1.12\ M_\odot$, $m_3 = 0.68\ M_\odot$, $a_1 = 6.47$ au, $a_2 = 177.68$ au, $e_1 = 0.157$, $e_2 = 0.512$, $i_{\rm tot} = 55.5°$.

In this case, we calculate the new orbital parameters of the tertiary star following Appendix A. If the mass-loss timescale is shorter than P_2, we use the impulsive approximation to estimate the new orbital configuration of m_3, as outlined in Appendix B. See Lu & Naoz (2019) for an analytic description of the post-kick orbital parameters.

The inner binary is followed in COSMIC with the following prescription, which depends on characteristic timescales. First, we define the remaining time in the simulation as $t_{\rm remain}$. Second, we consider the quadrupole level of approximation timescale in EKL (e.g., Antognini 2015), defined by:

$$t_{\rm EKL} = \frac{16}{30\pi}\frac{m_1 + m_2 + m_3}{m_3}\frac{P_2^2}{P_1}(1 - e_2^2)^{3/2}. \quad (2)$$

If $t_{\rm EKL} \geqslant t_{\rm remain}$, we assume the effects of the tertiary are negligible and run COSMIC for the remaining time. If $t_{\rm EKL} < t_{\rm remain}$, we evolve the binary in COSMIC until the mass-loss phase has ended. If the binary did not merge during this time, it is put back into triple-evolution code so long as it is no longer tidally locked and no longer experiencing Roche Lobe overflow. Figure 1 shows an example of such evolution.

In this Figure, we show the evolution of an inner binary with $m_1 = 1.09\ M_\odot$, $m_2 = 1.12\ M_\odot$, and outer companion $m_3 = 0.68\ M_\odot$. The figure focuses on the semimajor axis (black curve) and pericenter (light blue) evolution as a function of time, starting from 6 Myr. It also displays the change in the Roche limit (green) and radius (magenta) of m_2. The EKL eccentricity oscillations are clearly shown. The stars are driven into a tidally locked configuration as the eccentricity approaches 0 and the semimajor axis becomes smaller than four times the Roche limit of m_2. When this tidally locked state is reached, the system is evolved using COSMIC and is assumed to be decoupled from the tertiary. The semimajor axis evolution within COSMIC takes place only due to post-main-sequence evolution. The result is two WDs separated by 6 au. After recalculating the new orbital parameters for m_3 using the adiabatic prescription, the system is then evolved again using our triple-body code. The last panel is a zoomed-in on the final 1.3 Gyr of triple evolution.

During the COSMIC evolution, we also evolve the tertiary mass (m_3) using SSE to follow the change in stellar parameters as the inner binary evolves.

2.2. Initial Conditions

We choose two distinct ways to draw our initial conditions describing two different ansatzes. First, the inner and outer orbital periods are independently chosen from a lognormal period distribution with a mean of $\log(4.8/d)$ and a standard deviation of $\log(2.3/d)$ (Duquennoy & Mayor 1991). We then take the larger period to be the outer orbit and the smaller one to be the inner orbit. As the last step, we keep only systems that pass the stability criterion (described in Section 2.3). This procedure was used in Fabrycky & Tremaine (2007) and Naoz & Fabrycky (2014), thus allowing us to compare our results with them. We label this set of runs as "IB" (independent binary) because, for unstable systems, both the inner and outer period distributions are resampled. Rose et al. (2019) and Stegmann et al. (2022) showed that the final distribution of periods (as well as eccentricity) is highly correlated with the initial distribution. Thus, motivated by these results and the observations of Duquennoy & Mayor (1991), we adopt the observed period and eccentricity distributions from Duquennoy & Mayor (1991) as the initial distributions of our systems. The semimajor axis of the inner and outer orbits from this scenario is shown in the top panel of Figure 2.

The second channel draws the outer orbit from the Duquennoy & Mayor (1991) period distribution, and for that given outer period, continuously samples the inner orbit until a stable system is formed. This scenario assumes a hierarchy of formation. In other words, the outer orbit may have formed first, thus limiting the parameter space of the stable inner orbit. We note that because we later compare wide outer orbits with a tight inner orbit (in Section 4), we seek to compare both channels to the observations. We label this set of runs as "OB" (outer binary). The initial orbital separation of OB systems can be seen in Figure 2, bottom panel.

The eccentricity in both cases is chosen from a uniform distribution (consistent with Raghavan et al. 2010), the inclination is chosen from an isotropic distribution (uniform

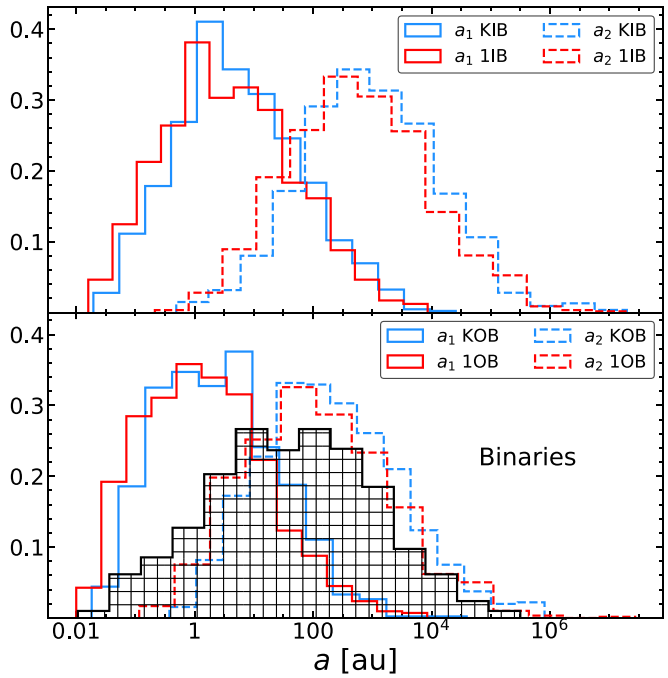

Figure 2. Initial inner ("in") and outer ("out") semimajor axis distributions of the triples for the *1OB*, *KOB* models (top), and *1IB*, *KIB* models (bottom). We also show the Gaussian curve used for our simulated binaries, which is again chosen from the period distribution of Duquennoy & Mayor (1991). This is to illustrate that the OB models had separation samples from this Gaussian curve; for details, see Section 2.2.

in $\cos i$), and the inner/outer argument of periapsis is chosen from a uniform distribution. The spin angle orbits are chosen from a uniform distribution for all runs. These orbital parameters are also sampled again with the orbital period during the resampling phase of both OB and IB models.

Further, we had two different choices for the initial masses. In the first, we chose, for both OB and IB cases, a mass value for m_1, m_2, and m_3 from the Kroupa initial mass function (IMF; Kroupa et al. 1993) ranging from 0.8 to 8 $M_\odot$ [6] (*KOB* and *KIB* runs). This allows us to produce many WDWD binaries. These models also assume that the mass of the tertiary is independent of the mass of the inner binary, which is consistent with observations of wide binaries (Moe & Di Stefano 2017).

To compare to Fabrycky & Tremaine (2007) and Naoz & Fabrycky (2014) we also adopt a set of runs where $m_1 = 1\ M_\odot$ initially (*1OB* and *1IB*, runs). These runs allow us to produce a robust sample of WDMS binaries. The mass ratio m_2/m_1 ($m_3/(m_1+m_2)$) for the inner (outer) orbit is chosen from Duquennoy & Mayor (1991), adopting a Gaussian distribution with a mean of 0.23 and a standard deviation of 0.42. These models assume that the masses between the binaries are correlated. Note that the literature also suggests that various initial mass ratio distributions are consistent with observations of WDMS binaries (Cojocaru et al. 2017). To explore these effects, we run two sets of adjacent simulations. In specific, we assume $m1 = 1\ M_\odot$, keep all other orbital elements the same as previously described, and run 250 simulations with a mass ratio selected from $n(q) \propto 1$ (uniform distribution) and 250 with $n(q) \propto q^{-1}$. Here, q is the mass ratio for both the inner and outer binary. After evolving these triples for 12.5 Gyr, we do not find any qualitative differences between the distributions of the final orbital parameters. We, therefore, omit these models from the paper to avoid clutter. The radii and spin of the stars are directly obtained from SSE.

We sample 1000 realizations for each of the four models (*1IB*, *KIB*, *1OB*, *KOB*), and provide the statistics in Table 1. A small fraction of the systems continued to run after two weeks of simulation time. Those runs have two categories; in one, they represent double WD (DWD) binaries exhibiting eccentricity and inclination oscillations after 10 Gyr. For these, we choose the final value for the systems to represent their endpoint (which is longer than 10 Gyr). These represent ∼1% of the systems. The other category represents systems that, after two weeks of running, are still below 12.5 Gyr time. They slowed down because stellar evolution or tides became important. These triples are omitted from the final sample, representing <1% of all systems.

We find that 46% of all triples become tidally locked, and 5% cross the Roche limit. After these have been put into COSMIC, 95% of outer parameters were updated according to adiabatic evolution, and only 5% used the kick protocol. Moreover, only 3% needed to be put back into the triple code again, after COSMIC's binary evolution.

Table 1
Descriptions of Different Simulations

Model	N Systems	m_1	(m_2,m_3)	SMA (a_1, a_2)	Close Bin.	Merged Bin.
1IB	978	1 $M_\odot$	DM91	DM91	16%	9 %
1OB	929	1 $M_\odot$	DM91	DM91*	24%	16%
KIB	938	K	K	DM91	6%	56%
KOB	943	K	K	DM91*	4%	54%
1Bin	850	1 $M_\odot$	DM91	DM91	27%	13%

Note. Close binaries are defined as those with final periods less than 16 days. "DM91*" means that a_2 was sampled from DM91, and for that fixed value of a_2, a_1 was sampled until a stable combination was formed (see Section 2.2).

2.3. Stability Criteria

For each set of sampled initial parameters, we require that the initial conditions satisfy dynamical and long-term stability. We adopt the hierarchical criterion ϵ, which describes the prefactor of the octupole level of approximation (e.g., Naoz et al. 2013a)

$$\epsilon = \frac{a_1}{a_2}\frac{e_2}{1-e_2^2} < 0.1. \quad (3)$$

The other stability criterion we use is (Mardling & Aarseth 2001):

$$\frac{a_2}{a_1} > 2.8\left(1+\frac{m_3}{m_1+m_2}\right)^{\frac{2}{5}}\frac{(1+e_2)^{\frac{2}{5}}}{(1-e_2)^{\frac{6}{5}}}\left(1-\frac{0.3i}{180^\circ}\right). \quad (4)$$

Note that deviation from hierarchy does not necessarily mean an instantaneous breakup of the system or instability. In fact, mildly hierarchical systems can still undergo large eccentricity excitations (Grishin et al. 2017; Bhaskar et al. 2020), and exhibit moderately long-term stability (Mushkin & Katz 2020; Zhang et al. 2023). However, here we consider a conservative

[6] Note that a lower mass limit will reduce the fraction of stars that end up as WDs. Because we are interested in the formation of WDs, we keep the minimum mass at 0.8 $M_\odot$, which will ensure that a large majority of the binaries will at least have one WD by the end of the simulation time.

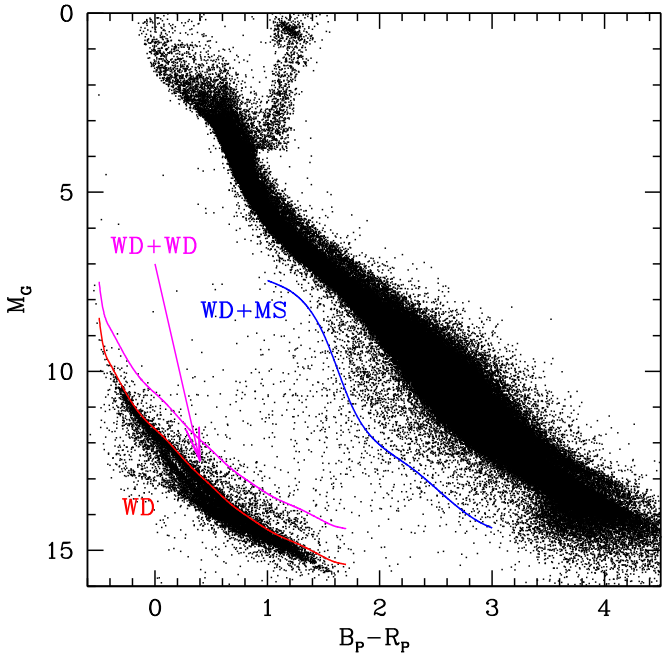

Figure 3. We display the flux–magnitude cutoffs used to gather our sample of observed Gaia binaries. Each point on this Gaia HR diagram represents a point source in the Gaia DR3 100 pc sample. For each source, we use the Gaia magnitude (M_G) as a function of the difference between the Gaia blue (B_p) and red (R_p) bands. Objects that lie to the left of the red line in Figure 3 are considered to be single WDs. Objects above the red curve and below the pink curve are identified as unresolved double WD binaries. The range between the magenta and blue lines is the region of WDMS binaries. For more information about the cutoffs, see Section 2.4.

approach and require only stable and hierarchical systems according to the aforementioned equations.

2.4. Gaia Observations

The general method of identifying WD triples using Gaia triples is by first identifying photometric binaries that contain a WD and then matching the binaries with a comoving companion (of any spectral type). Since we are searching for binaries as well, we do not impose any restriction on the RUWE parameter. After keeping only objects that have photometry for the G_p, B_p, and R_p Gaia bands and have an ASTROMETRIC-ERROR <0.9, we begin our search for WD systems using a Gaia Hertzsprung–Russell (HR) diagram (Figure 3). Objects that lie to the left (blueward) of the red line in Figure 3 are considered to be single WDs. This criterion is determined empirically by marking the edge (FWHM) of the number counts as a function of color for a fixed M_G bin. Objects that lie above this line are too bright to be a single WD of normal mass at this color and are therefore likely to be an unresolved double WD—a photometric binary. In principle, these objects could also be unusually low-mass single WDs, but such objects are believed to be the result of close binary evolution anyway, and so still satisfy our criterion. Therefore, we define a second criterion—the magenta line—which lies 1 magnitude brighter than the red line. In between these two criteria, we count objects as photometric double WD binaries. This criterion is similar to the one used in Inight et al. (2021).

WDs may also be in close binaries with main-sequence stars as well. For upper main-sequence stars, the companion flux would completely overwhelm the WD, and these objects are not identifiable by photometry alone. For low-mass main-sequence companions, the WDMS pairs lie between the WD sequence and the main sequence. We, therefore, consider the range between the magenta and blue lines to be the region of WDMS binaries. The blue line was generated empirically to remove the "reverse binary sequence" observed below the main sequence in Figure 3. Closer inspection of these objects indicates that they represent blends between foreground stars and distant background objects in crowded regions of the sky, so we exclude this region from the sample selection. Our selection method for WDMS systems is similar to Rebassa-Mansergas et al. (2021).

Any catalog of WDMS systems will be significantly incomplete because WD are much fainter than upper MS stars and will not change their colors if added together in a photometric binary. To quantitatively assess the level of uncertainty, we construct luminosity functions from the single WD and MS populations and then construct a model WDMS population by randomly sampling from both single populations. For the 26% of the resulting sample that contains MS stars with $M_G < 7$, not even hot WDs are sufficient to generate photometric binaries that fall within our WDMS region. Only 16% of the model photometric binaries fall within our WDMS region. Furthermore, we have verified that very few WDMS pairs are blue enough to fall within the WDWD photometric cut. Only 0.7% of our sample falls within this bin—most importantly, the comparison between the samples defined by our DWD and WDMS cuts implies that the contamination of the DWD sample by the WDMS sample should be only 4% of the WDMS sample itself.

Despite the low absolute completeness of our WDMS sample, however, the incompleteness is not a major issue in this calculation because our interest is only in comparing the separations of the DWD and WDMS binaries, in relative terms. We are therefore assuming that completeness does not highly correlate with the separation of the outer pair in the triple. See Appendix D for more details on our methods of assessing contamination.

By comparing these $B_p - R_p$ flux–magnitude values (Figure 3), we identify approximately 60,000 single WDs, 11,000 DWDs, and 44,000 WDMS pairs in the 200 pc Gaia sample. We note that the other surveys, including those for double WDs (e.g., Inight et al. 2021; Rebassa-Mansergas et al. 2021; Torres et al. 2022), are consistent with the estimations in Figure 3.

Once the inner binaries are established, we identify those with a comoving companion, which would then upgrade the system to a triple. To find these companions, we first require that their distances are consistent with that of the identified primary to within 10% and to within 2σ, where σ is the largest of the two distance error bars. For each system, we then calculate the projected separation ($R_\perp$), relative projected velocity ($V_\perp = V_2 - V_1$), and relative projected angle between the velocities (θ). We require that $\cos(\theta) > 0.99$ to ensure that the vectors are pointing in the same direction, and we exclude any object that matches more than two other objects in the Gaia catalog. Lastly, quantifying the El-Badry et al. (2021) velocity criterion, we require the two objects to be in a bound orbit using the empirical criterion: $V_\perp < 67{,}000\ \mathrm{km\ s^{-1}} (R_\perp)^{-1.2}$, where $R_\perp$ is in au. This criterion is more relaxed than inclusion criteria based on expected relative velocities for a bound Kepler orbit, but we wish to account for the possibility that the relative motion of the common proper motion pair—the outer pair of a

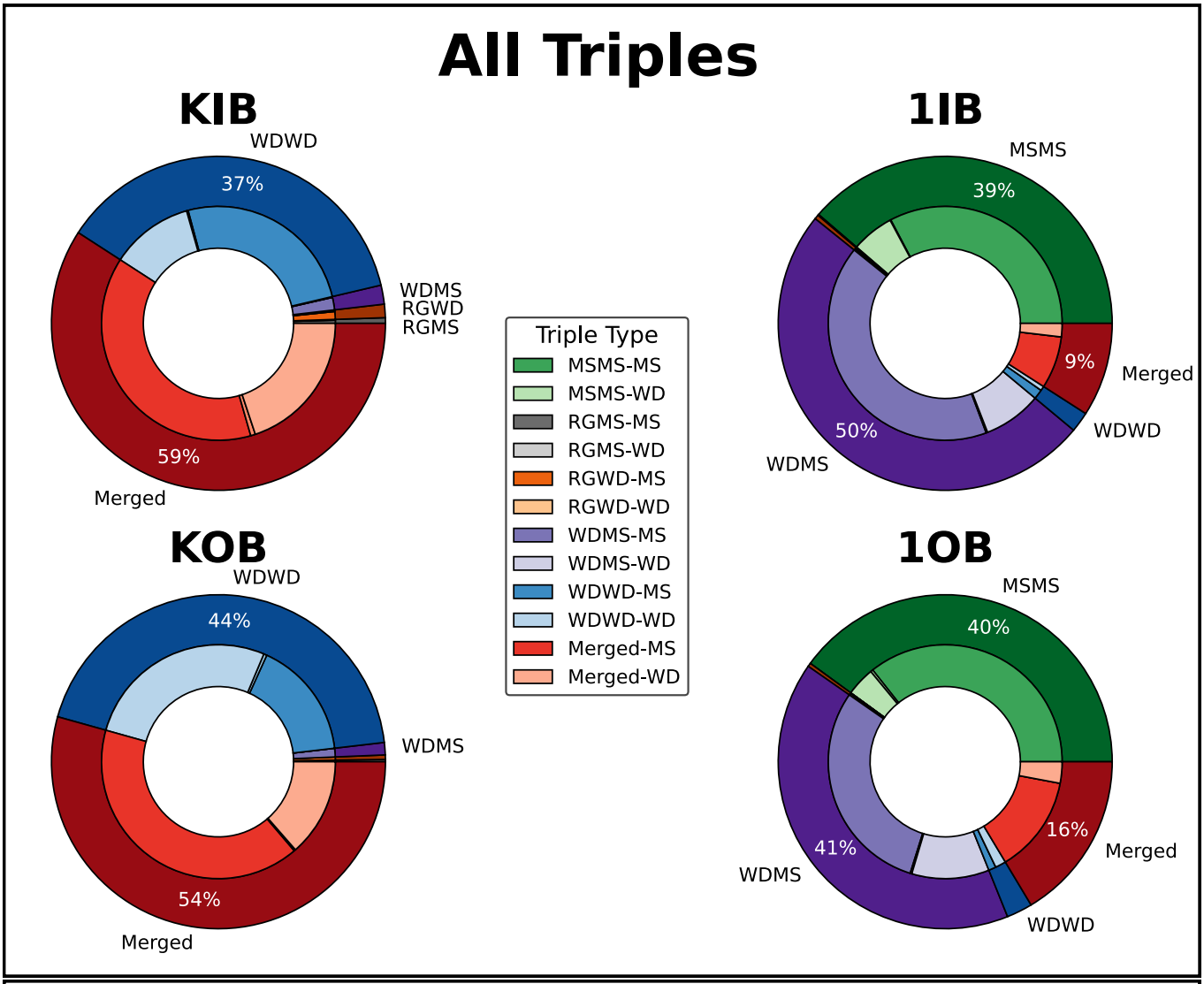

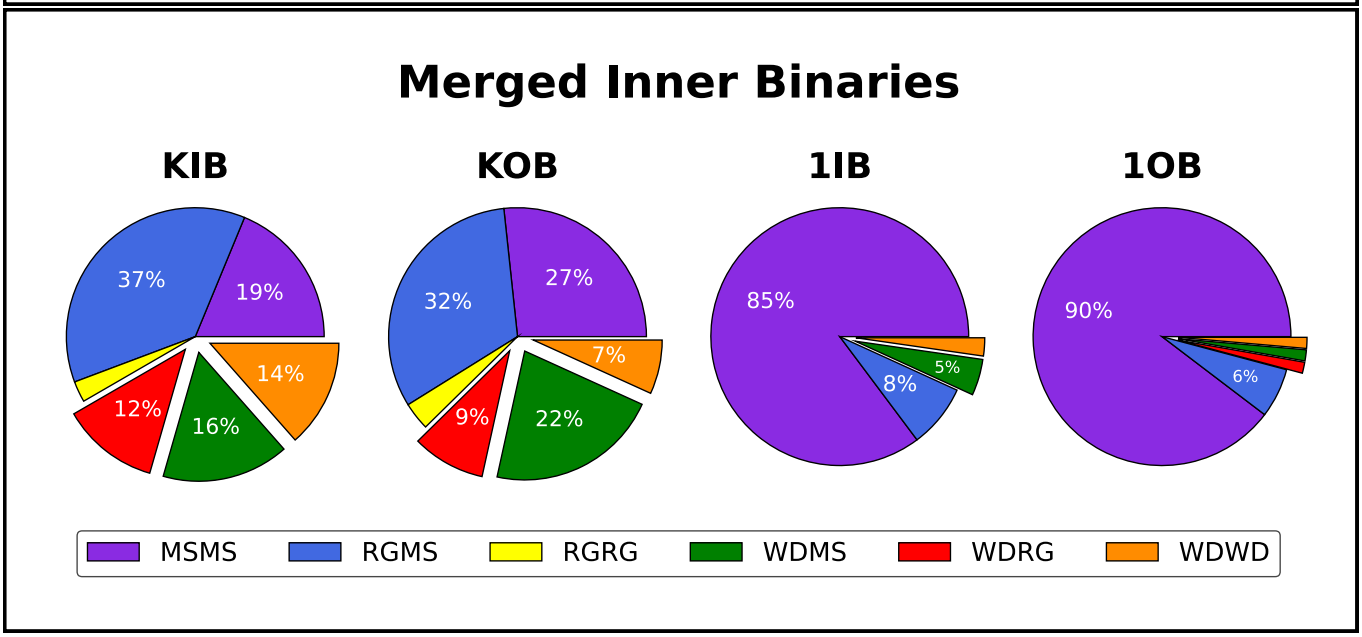

Figure 4. The types and fractions of the different triples (top) and mergers (bottom) produced from the three-body simulations. Top: the outer ring represents the type of the inner binary, and the inner ring specifies the type of the third star. The color corresponding to the type of triples is outlined in the legend, where MS is for main-sequence star, RG is for red giant, and WD is for WD. Bottom: distribution of different stellar types of the inner binary before the merger event. The exploded slices correspond to mergers that included at least one WD.

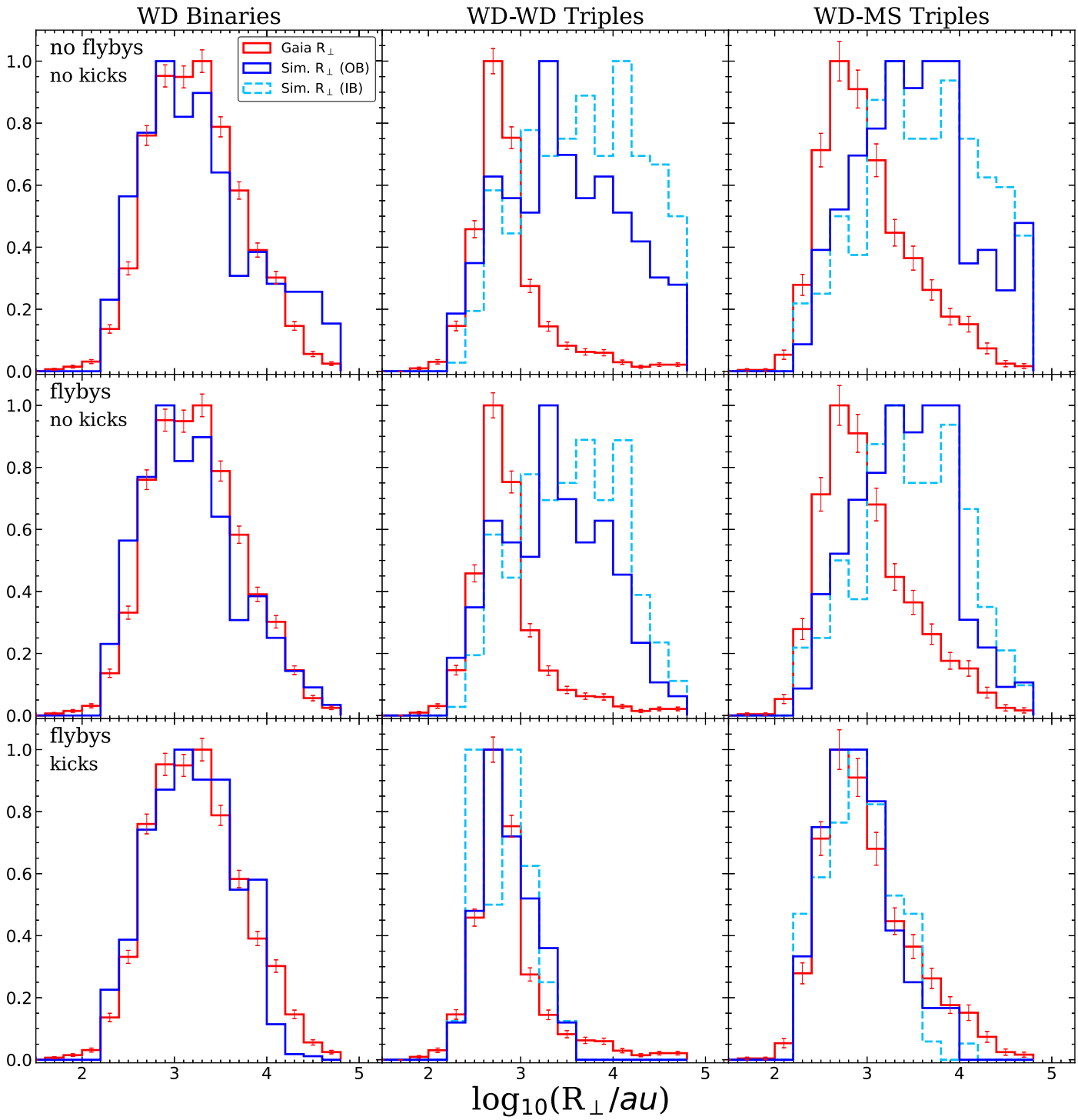

Figure 5. The separation distribution of simulated triples compared to the observed Gaia 200 pc sample. We compare the projected separations ($R_\perp$) between the inner binary and the tertiary of Gaia triples (red) to the final outer semimajor axes $R_\perp$ of the simulated triples. The solid blue curve is the result of our outer binary (OB) models, and the dashed light blue curve is the result of the independent binary (IB) models (Section 2.2). We explore the effects of both flyby interactions and mass-loss-induced kicks in changing the separation distributions. The first row shows the raw outcome of simulations, without the inclusion of any perturbative mechanisms. The second row takes into account the effect of flyby interactions in unbinding wide triples (e.g., Michaely & Perets 2020). The bottom row takes into account both flyby interactions and the effect of mass-loss-induced kicks in changing the outer separation (a_2) of triples (following El-Badry & Rix 2018). See Section 4 for a detailed comparison between the observed and theoretical samples. For information on how flybys and kicks were incorporated into our simulated triple systems, we refer the reader to Sections 4.2.1 and 4.2.2. Note the agreement between the Gaia distribution and the simulation results in the bottom row.

triple—may be influenced by partially resolved relative motion within the binaries—the inner pair of a triple. The upper limit on the width of the triple is $R_\perp < 10^5$ au.

Overall, we find a total of 3913 WD binaries, 1235 triples with an unresolved WDWD inner binary, 2286 triples with an unresolved WDMS inner binary, and 87 triple WDs. In

Section 4 we compare this observed sample to our simulated population of WD triples.

3. Analysis and Results

3.1. Triple Types

The specific types of resultant triples from our simulations, along with their fraction, are displayed in Figure 4. In this Figure, the first four letters describe the stellar types of the inner binary, and the last two letters describe the type of the tertiary star (m_3). For example, WDMS-RG describes a triple with an inner WDMS binary orbited by a red giant (RG) tertiary star.

As expected, we find that the Kroupa IMF models (*KIB* and *KOB*) produce a greater frequency of DWD inner binaries. These models also generate more mergers, mainly due to the accelerated evolution from the larger initial masses. For the $m_1 = 1\ M_\odot$ models (*1IB* and *1OB*), we find, by design, that the final binaries are mainly WDMS, with a smaller fraction of merged binaries.

3.2. Outcomes

Figure 4 summarizes the outcomes of our simulations. Notably, a sizable fraction of triples merged, especially in the Kroupa IMF models (*KOB* and *KIB*). These were a mix of high eccentricity EKL mergers (∼47%), and those that reached a common envelope stage during the post-main-sequence evolution (∼53%). We categorize the merged binaries based on the stellar types of the binaries in the bottom panel of Figure 4.

Focusing again on the Kroupa IMF models, Figure 4 shows that 37% and 44% of DWD triples from the *KIB* and *KOB* models, respectively, remained in a triple configuration for the full 12.5 Gyr. The *KIB* runs assumed an independent choice of the inner binary's initial period, while the *KIB* model chose a fixed sample of the initial outer period before sampling the inner one. See Figure 2 for the distribution of initial separations for both *KIB* and *KOB* and Section 2.2 for a description of the different models.

As seen in Figure 4, DWDs are associated with both WD or MS stellar companions. We note that the tight DWD circular binaries ($a_1 \lesssim 0.1$ au) are often associated with both WD and MS companions at a wide range of distances (see Appendix C Figure 6). About 7% of all DWD systems exhibit such tight configurations. The rest, as expected, undergo EKL eccentricity oscillations, although, at this point of the evolution (>10 Gyr), these are not expected to reach high values. This is because high eccentricity events (due to the octupole level of approximation) would have already taken place.

4. Comparison to Gaia

4.1. Setup for the Comparison

We compare the population of our simulated WD triples to the local 200 pc Gaia sample in Figure 5 (see Section 2.4 for details on the sample). In Figure 5, we compare the distribution of projected separation between the inner orbit and tertiary star ($R_\perp$) of our simulated WD triples to the $R_\perp$ of WD triples from Gaia. For the simulated WD systems, we calculate the $R_\perp$ between the inner binary and m_3 by relating it to the semimajor axis of the outer orbit (a_2) using $R_\perp = a_2/1.10$. This relation is derived from Dupuy & Liu (2011), who show that, for uniform eccentricities, the conversion factor between the semimajor axis of a binary, a, and the projected separation, $R_\perp$, can range from $a/R_\perp = 0.75 - 2.02$ for 1σ uncertainty, with a median conversion factor of $a/R_\perp = 1.10$. We apply the median conversion factor to convert the simulated a_2 to the $R_\perp$ values from Gaia. The first, second, and third columns compare the simulated and observed distributions for WD binaries (model *1OB*), WDWD triples, and WDMS triples, respectively.

Specifically, the observed distribution from Gaia is plotted in red with Poisson error bars. We then compare this distribution to simulations by aggregating the models based on their initial periods. We combine the models with independent choices of the inner binary's initial period (*1IB* and *KIB*) in solid blue, and those where the outer binary was chosen first (*1OB* and *KOB*) in dashed light blue.

For the comparison, we only include simulated triples that exhibit $a_1 < 200$ au and 200 au $< a_2 < 10^5$ au, to match the observational limitations in the Gaia sample (see Section 2.4). The restriction on a_1 represents the widest inner binary such that it can still be observed as a point source at a distance of 200 pc with Gaia's angular resolution of $0\farcs43$ (Gaia Collaboration et al. 2016). This is the nominal Gaia angular resolution value, though larger values have been proposed for WD binaries (e.g., Torres et al. 2022). We find that such an increase in angular resolution has minimal implications for our comparisons. We investigate the effects of varying angular resolutions with more detail in Appendix D We also note that our method of identifying hierarchical WD triples (see Section 2.4) may have a smaller sample of massive DWDs or WDMS binaries with cool WDs. The former is not a major issue because most of our DWD triples have inner binaries with each WD having a mass less than 1 $M_\odot$.

4.2. Internal and External Perturbations

In order to accurately compare our isolated WD systems to field triples from Gaia, it is crucial that we account for two additional dynamical perturbations: flyby interactions and mass-loss-induced kicks (e.g., Hamers & Thompson 2019). We outline the imprints of both mechanisms in the sections that follow.

4.2.1. Flyby Kicks

The Galactic field is known to be collisional for wide systems with $a > 10^3$ au (e.g., Kaib & Raymond 2014; Michaely & Perets 2016, 2019, 2020; Hamers & Thompson 2019). Over the 12.5 Gyr evolution time, we can expect the wide orbits to experience many weak encounters from field stars. The encounters can serve to (1) ionize wide triples or (2) change the periastron of the outer binary through eccentricity pumping (Michaely & Perets 2016). The latter effect can cause a disruption event in the inner binary during the pericenter passage, leading to unstable (or potentially unbound) triples. This effect is more emphasized for wider inner binaries, which exhibit larger loss cone radii. Michaely (2021) specifically studied the effects of flyby interactions in the field on wide WD triples. They show that, for initially wide triples ($a_2 > 10^4$ au), there is a non-negligible probability that flyby interactions will destabilize and potentially unbind the triple in ∼10 Gyr. To account for the effect of ionization of wide triples due to flyby interactions in our sample, we calculate the half-life of the outer binaries following Bahcall et al. (1985) and Michaely & Perets (2020). We take the mass of the perturber star to be 0.5 $M_\odot$, the

local stellar number density to be $n_* = 0.1$ pc^{-3} (Holmberg & Flynn 2000), and an encounter velocity of $v_{\rm enc} = 50$ km s^{-1}.

Finally, we divide the half-life by the total evolution time to find the probability that the triple will survive after 12.5 Gyr. If the half-life is greater than the 12.5 Gyr integration time, we take the probability of survival to be 1. The height of each bin in the middle row of Figure 5 is scaled by the probability of survival, which suppresses the survivability of ultrawide triples. We also expect another fraction of these triples, especially those with wider inner binaries, to become unstable due to the effect (2). However, unbinding caused by disruption at the pericenter is a less significant phenomenon that is neglected here (Michaely & Perets 2020).

We note that galactic tides can also play a role in disrupting systems in the galactic field with separations larger than 10^4 au (Kaib & Raymond 2014; Grishin & Perets 2022). Such effects are neglected because most of these wide binaries already become unbound due to the other two effects.

4.2.2. Mass-loss Kicks

A major internal dynamical effect that could lead to the unbinding or widening of triples is the prospective kicks induced by the post-MS evolution of the inner binary. Previous studies have shown that velocity kicks during post-MS evolution, presumably due to asymmetric mass loss during WD formation, can unbind wide ($a > 10^3$ au) systems in the galactic field (Savedoff 1966; Fellhauer et al. 2003; Toonen et al. 2017; El-Badry & Rix 2018).

These kicks will vary in magnitude based on the mass of the WD progenitor but will be on the order of 0.75 km s^{-1} (e.g., El-Badry et al. 2018). Such an effect was shown to unbind most field binaries with $\log(a/\mathrm{au}) > 3.5$, and lead to a greater correlation with the observed distribution of local Gaia binaries (El-Badry & Rix 2018). Following this work on binaries, Hamers & Thompson (2019) investigated the effect of both flyby's and WD kicks on triples. When accounting for both WD kicks and flyby's, up to 50%–60% of their triples became unbound in 10 Gyr.

Following El-Badry & Rix (2018), we assumed that each WD formed in a triple produced a mild, instantaneous kick with velocity $v_{\rm kick}$. The magnitude of this kick was chosen from the Maxwellian distribution

$$P(v_{\rm kick}) = \sqrt{\frac{2}{\pi}}\,\frac{v_{\rm kick}^2}{\sigma_{\rm kick}^3}\exp\left[-\frac{v_{\rm kick}^2}{2\sigma_{\rm kick}^2}\right], \tag{5}$$

which uses a standard deviation $\sigma_{\rm kick} = 0.5$ km s^{-1} and peaks at $v_{\rm kick} = \sqrt{2}\,\sigma_{\rm kick} \approx 0.75$ km s^{-1} (El-Badry & Rix 2018). The impact of a natal kick in changing the separation in a system is highly dependent on the direction of the kick and the orbital phase of the companion during the kick.

For each WD in a triple, we sample one kick velocity ($v_{\rm kick}$) from the probability distribution in Equation (5). For the chosen kick velocity, we sample the direction of the kick and the eccentric anomaly of the tertiary star 1000 times, both from a uniform distribution. Then, for each of the 1000 trials, we calculate the new semimajor axis of the companion (a_2) assuming an instantaneous natal kick (see Appendix B for the relevant equations, based on Lu & Naoz 2019). If more than half of these a_2 values led to unbound orbits, we conclude that the kick has ionized the orbit. Otherwise, we choose the median a_2 from all samples (that kept a bound orbit) to be the new a_2 after the post-WD kick.

Including the effect of mass-loss-induced kicks leads most triples with $\log(a_2/\,\mathrm{au}) > 3.5$ to become unbound (bottom row of Figure 5). Before kicks were applied to the systems (first and second row of Figure 5), we find that the WD binaries had consistent distributions with Gaia, while the WD triples did not. This consistency with binaries suggests that our underlying model—without kicks—is reasonable. Therefore, the disagreement with the distribution of triples in this panel, and the fact that there is an agreement in the bottom panel, strengthens the argument for the presence of mass-loss kicks during the evolution of triple-stellar systems.

Kicks more strongly affect DWD triples, because they undergo, at minimum, two kicks during their evolution. The steeper decline in separation distribution for observed DWD triples, compared to WDMS triples, may be attributed to this phenomenon. Namely, the scarcity of wide DWD triples (relative to the number of wide WDMS triples) in our Gaia field sample may be from their unbinding due to the extra WD kick.

Note that some agreement between the Gaia sample and our simulations can be also reached by only considering systems where the initial outer-orbit semimajor axis satisfies $a_2 \lesssim 1250$ au.

5. Discussion and Conclusions

The recent Gaia Data Release 3 has observed hundreds of thousands of WDs with unprecedented accuracy (Gentile Fusillo et al. 2019, 2021). Provided that a significant fraction of these WDs have companions (Hollands et al. 2018), Gaia observations give us a unique opportunity to test our theoretical framework of triple-stellar dynamics on long ($\geqslant$10 Gyr) timescales.

In this study, we thoroughly examine stellar three-body systems as they evolve into WD triples. We perform detailed Monte Carlo simulations, where we dynamically evolve thousands of stellar triples for over 10 Gyr while incorporating, hierarchical three-body secular evolution of the orbits, GR precession, tides, and stellar evolution. Moreover, we track phases of mass loss and the common envelope of the inner binary.

We leverage Gaia DR3's data on WDs in triple configurations (see Figure 3) to compare the separation distribution of our simulated WD triples to a 200 pc sample from Gaia. We find that the DWD-tertiary and WDMS-tertiary separation distributions are consistent with the Gaia sample if mass-loss kicks are considered. These small kicks ($v_{\rm kick} \sim 0.75$ km s^{-1}) may be produced during WD formation (El-Badry & Rix 2018) or otherwise. Their specific origin is kept agnostic in the analysis.

Given the aforementioned agreement, we predict that ~30% of all solar-type stars were born in triples. We derive this estimate by leveraging the statistics from the Kroupa IMF models (*KIB* and *KOB*). Out of our simulated systems, 55% had their inner binaries merge within the 12.5 Gyr. Of the surviving ones, 92.5% ended up in a DWD-tertiary configuration, and lastly, of those systems, 61% became unbound due to mass-loss kicks. Thus, comparing these to the 1235 DWD triples candidates that are observed today in the local 200 pc from Gaia (see Section 2.4), we find $7719 = 1235/0.16$ DWD triple-progenitors initially. Given the estimated local stellar

density (i.e., $n_* = 0.1$ pc^{-3}; Holmberg & Flynn 2000) we find that ∼30% of all WD progenitors were born in triples.

Moreover, Heintz et al. (2022) recently showed that 21%–36% of wide (>100 au) DWDs were likely once triples. They consider the cooling ages of observed WDs in binaries from Gaia and find shorter cooling ages than would be predicted from the isolated evolution of a WD. This observation is interpreted as evidence of prior mergers or the presence of an unresolved companion. Specifically, these markers would suggest that some fraction of the observed Gaia DWDs—as described in Section 2.4—were also once triples. Combining their result with the mentioned fraction of triples estimated from the agreement in Figure 5 suggests that the fraction of Sun-like stars that were born in triples may be even larger, i.e., ⩾40%.

We note that this fraction is consistent with previous estimates in our local neighborhood (e.g., Tokovinin 1997; Pribulla & Rucinski 2006). Moreover, the triple-body evolution also yields many mergers, particularly from the two models, and we find that ∼22% of all triples lead to a merger containing at least one WD. Specifically, these consist of 10% WDMS mergers, 6% of DWD mergers, and 6% of WDRG mergers. The WD merger events may result in (either single or double degenerate) Type Ia supernovae (e.g., Raskin et al. 2009; Rosswog et al. 2009; Hawley et al. 2012; Hamers et al. 2013, 2018; Toonen et al. 2018; Michaely & Perets 2020; Michaely & Shara 2021; Liu et al. 2023) and cataclysmic variables (CVs; e.g., Nelemans et al. 2001; Knigge et al. 2011; Pala et al. 2017). We thus predict ∼1698 such systems within 200 pc over the last 10 Gyr. Note that our estimate was derived assuming that all stars were born around the same period of time.

Double WD binaries are also predicted to be the most numerous gravitational-wave (GW) sources detectable by LISA (e.g., Marsh 2011; Amaro-Seoane et al. 2017). Specifically, tight or merging DWDs, are expected to be abundant in the mHz LISA bands (Korol et al. 2017; Kupfer et al. 2018; Burdge et al. 2019; Li et al. 2020; Xuan et al. 2021). We find the strain curves and signal-to-noise ratio for each of our DWD systems, relative to the LISA strain curve. Here, we assume our sources to be 200 pc. away, the GW emission to be sinusoidal, and the observation time to be 4 yr (the minimum for LISA Amaro-Seoane et al. 2017). We find that 14% (∼172 within the local 200 pc) of DWDs have a signal-to-noise ratio greater than 5, making them visible in the LISA mHz band.

Acknowledgments

We thank the anonymous referee for constructive feedback on the manuscript. We thank Zeyuan Xuan for useful discussions regarding the gravitational-wave implications of close DWD binaries. C.S. thanks the UCLA Undergraduate Research Fellows Program. S.N. acknowledges the partial support from NASA ATP 80NSSC20K0505 and from the NSF-AST 2206428 grant, as well as thanks Howard and Astrid Preston for their generous support.

Appendix A
Adiabatic Change in Outer Orbital Parameters

For binaries that evolved in COSMIC for longer than P_2, we calculate the new e_2 and a_2 assuming adiabatic (slow and isotropic) mass loss. Namely, we assume that e_2 does not change, and calculate the new a_2 from

$$a_{2,f} = \frac{M_i}{M_f} a_{2,i}, \tag{A1}$$

where M_i is the total mass of the triple before it was inputted into COSMIC, M_f is the total final mass of the system, and $a_{2,i}$ is the outer semimajor axis before the binary is inputted into COSMIC. We calculate the new mutual inclination (i_f) using

$$\cos(i_f) = \frac{G_{\rm tot}^2 - G_{1,f}^2 - G_{2,f}^2}{2G_{1,f}G_{2,f}}, \tag{A2}$$

where $G_{1,f}$ ($G_{2,f}$) is the final orbital angular momentum of the inner (outer) binaries, and $G_{\rm tot}$ is the total orbital angular momentum of the triple (Naoz 2016). For adiabatic mass loss, we assume $G_{2,f}$ to change according to

$$G_{2,f} = \frac{\mu_{2,f}}{\mu_{2,i}} G_{2,i}, \tag{A3}$$

where $\mu_2 = (m_1 + m_2)m_3/(m_1 + m_2 + m_3)$ is the reduced mass of the outer binary.

Appendix B
Post-kick Outer Orbital Parameters

For binaries that evolved in COSMIC for less than P_2, we calculate the new e_2 and a_2 by assuming an inner binary to produce a kick in the outer orbit. We follow the procedure for binaries outlined in Lu & Naoz (2019), and use the subscript "1" for the inner orbit, "2" for the outer orbit, and "n" for the post-kick parameters.

First, we calculate the magnitude of the position vectors of the inner (1) and outer (2) orbits by using

$$r_i = a_i(1 - e_i \cos E_i), \ i \in \{1, 2\}. \tag{B1}$$

Here, the eccentric anomaly (E_i) is uniformly sampled for both orbits. The magnitude of the outer orbital velocity is then given by

$$V_2 = \sqrt{\mu\left(\frac{2}{r_2} - \frac{1}{a_2}\right)}, \tag{B2}$$

where $\mu = k^2(m_3 + m_1 + m_2)$. Then, after defining $\beta \equiv \frac{m_3 + (m_{1,n} + m_{2,n})}{m_3 + (m_1 + m_2)}$, and assuming that the kick velocity (u_k) is 0, we apply Equations (10), (19) from Lu & Naoz (2019) to get the new SMA and eccentricity:

$$a_{2,n} = a_2 \frac{\beta(1 - e_2 \cos E_2)}{2\beta - (1 + e_2 \cos E_2)(1 + u_k^2 + 2u_k \cos\theta)} \tag{B3}$$

$$e_{2,n}^2 = 1 - \frac{r_2^2 V_2^2}{k^2(m_3 + m_{1,n} + m_{2,n})a_{2,n}}. \tag{B4}$$

Where we have chosen $r_2 \perp V_2$.

Appendix C
Trends in Orbital Parameters

We consider systems that kept their triple nature by the end of the run, meaning the inner binary did not merge. Figure 6, depicts the orbital parameters of these triples. In particular, the top panels show the orbital separation of the outer binary (a_2) as a function of the inner binary's separation (a_1). The bottom

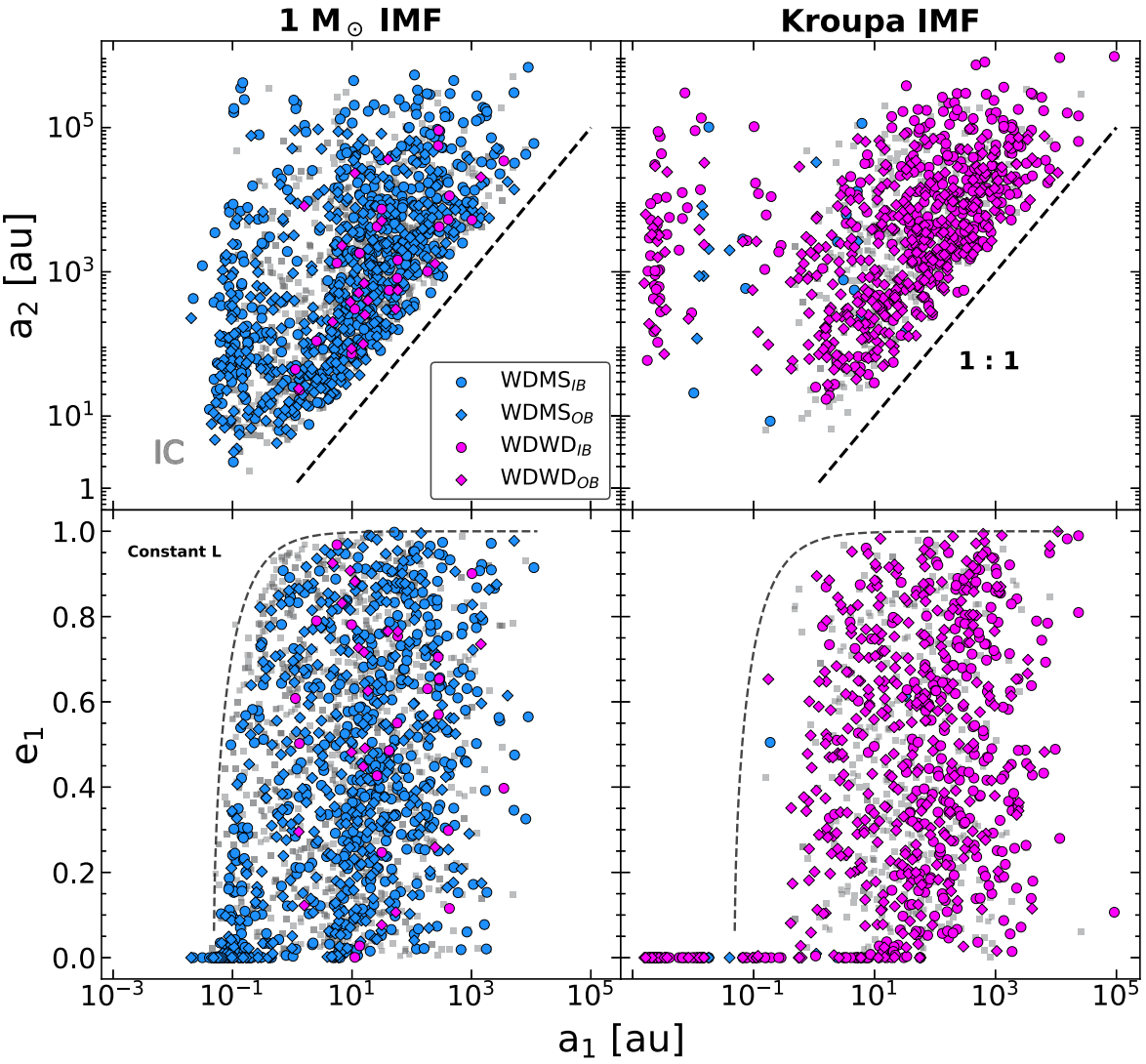

Figure 6. The outer-orbit separation (a_2, top row) and the inner eccentricity (e_1, bottom row), as a function of the inner semimajor axis (a_1) for all WD triples. The right column depicts the *1IB* and *1OB* runs, for which $m_1 = 1\ M_\odot$ initially, while the left panel plots the models with Kroupa IMFs (i.e., *KIB* and *KOB* runs). We show WDMS binaries in blue and WDWD binaries in magenta. Circles represent binaries from the *1IB* and *KIB* models; diamonds represent binaries from the *1OB* and *KOB* models. Gray squares show the initial conditions (IC). The dashed black in the top panel shows the $a_1 = a_2$ (1:1) line. In the bottom row, the dashed black line shows a constant angular momentum curve.

panels show the inner orbit's eccentricity (e_1) as a function of a_1. The gray light markers show the initial conditions. The different colors correspond to the type of inner binary, where WDMS binaries are plotted in blue, and WDWD binaries are in magenta. The circular scatter points correspond to triples from the models where the initial periods were chosen independently (*1IB* and *KIB*). The diamond markers refer to triples from the models where the outer orbit's initial period was chosen first (*1OB* and *KOB*). The left column plots only triples from the 1 $M_\odot$ models (*1IB* and *1OB*), and the right column is for the Kroupa IMF models (*KIB* and *KOB*). See Section 2 for a complete description of the different models and initial conditions used.

In this figure, the Kroupa IMF models lead to a greater fraction of tight, circularized WDWD binaries ($a_1 < 0.1$ au). Interestingly, these close binaries are associated with companions at a wide range of separations.

Appendix D
Impact of Angular Resolution on Gaia Sample

In our analysis, we adopt the nominal Gaia angular resolution value of 0.″43 (Gaia Collaboration et al. 2016). Recent studies (e.g., Torres et al. 2022) estimate that the angular resolution can reach values closer to 2.″5. To assess the impact of the angular resolution on our sample, we investigate the completeness of all photometric pairs within 200 pc. We test the resolution limit by plotting the cumulative distribution of angular separations for all matched pairs within 200 pc, shown in the solid curve). This curve includes everything, not just WDs. We then compare this distribution to the dotted curve, which is the best-fit Gaussian to our theoretical separation distribution (blue histogram in Figure 5). The Gaussian is described by

$$n(R) = e^{-0.5(\log(R)-3.15)^2/0.22}. \quad \text{(D1)}$$

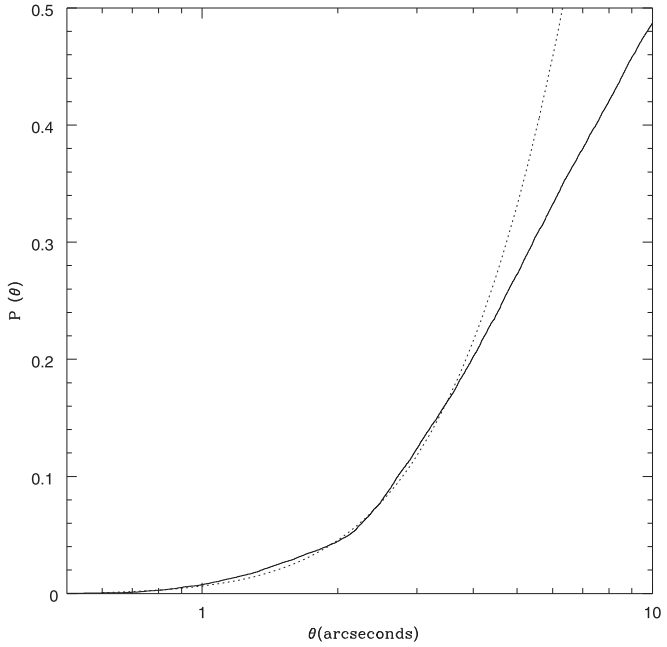

Figure 7. The cumulative distribution function of angular separations for all matched pairs within 200 pc in the Gaia catalog (solid line) compared to the analytic model (dotted) outlined in Equation (D1).

Assuming volume completeness out to 200 pc, we then convert this separation distribution to an angular resolution distribution (dotted curve in Figure 7). The dotted curve is an exceptional fit to the solid curve at short separations, suggesting that our angular resolution assumptions are sound.

As noted above, the specified DWD and WDMS regions identified in Figure 3 may be contaminated by other systems. To assess photometric completeness in our sample, we employ a Monte Carlo approach. First, we isolate the single WD and MS using the cuts specified for our single-star cutoffs (see Section 2.4). We then sample both populations and add them together to make an unbiased sample of model WDMS and DWD binaries. We then examine which one of these binaries entered our color–magnitude cuts for the different object types. 25.5% featured an MS star with $M_G < 7$, so they are excluded from the sample. 58.3% featured a WDMS binary, but the WD was too faint and it remained rightward of the blue curve in Figure 3. A total of 15.5% made it into the region between the blue and magenta curves (i.e., our WDMS binaries). 0.66% made it into the double white dwarf region (between magenta and red curves), and 0.036% made it into the single white dwarf region (left of the red curve). Only 4% of the WDMS sample makes it into the WDWD region, meaning that about 1760 of the 11,000 DWD might be WDMS. As mentioned in Section 2.4, our sample does miss WDs around bright MS stars, but this issue is not severe since the contamination fraction is small.

ORCID iDs

Cheyanne Shariat https://orcid.org/0000-0003-1247-9349
Smadar Naoz https://orcid.org/0000-0002-9802-9279
Bradley M. S. Hansen https://orcid.org/0000-0001-7840-3502
Isabel Angelo https://orcid.org/0000-0002-9751-2664
Erez Michaely https://orcid.org/0000-0002-9705-8596
Alexander P. Stephan https://orcid.org/0000-0001-8220-0548

References

Amaro-Seoane, P., Audley, H., Babak, S., et al. 2017, arXiv:1702.00786
Angelo, I., Naoz, S., Petigura, E., et al. 2022, AJ, 163, 227
Antognini, J. M. O. 2015, MNRAS, 452, 3610
Bahcall, J. N., Hut, P., & Tremaine, S. 1985, ApJ, 290, 15
Bhaskar, H., Li, G., Hadden, S., Payne, M. J., & Holman, M. J. 2020, AJ, 161, 48
Blouin, S. 2022, A&A, 666, L7
Blouin, S., & Daligault, J. 2021, ApJ, 919, 87
Blouin, S., Daligault, J., Saumon, D., Bédard, A., & Brassard, P. 2020, A&A, 640, L11
Breivik, K., Coughlin, S., Zevin, M., et al. 2020a, ApJ, 898, 71
Breivik, K., Mingarelli, C. M. F., & Larson, S. L. 2020b, ApJ, 901, 4
Burdge, K. B., Coughlin, M. W., Fuller, J., et al. 2019, Natur, 571, 528
Chandra, V., Hwang, H.-C., Zakamska, N. L., & Cheng, S. 2020, ApJ, 899, 146
Cheng, S., Cummings, J. D., & Ménard, B. 2019, ApJ, 886, 100
Cheng, S., Cummings, J. D., Ménard, B., & Toonen, S. 2020, ApJ, 891, 160
Cojocaru, R., Rebassa-Mansergas, A., Torres, S., & García-Berro, E. 2017, MNRAS, 470, 1442
Dupuy, T. J., & Liu, M. C. 2011, ApJ, 733, 122
Duquennoy, A., & Mayor, M. 1991, A&A, 248, 485
Eggleton, P. P. 1983, ApJ, 268, 368
Eggleton, P. P., Kiseleva, L. G., & Hut, P. 1998, ApJ, 499, 853
El-Badry, K., & Rix, H.-W. 2018, MNRAS, 480, 4884
El-Badry, K., Rix, H.-W., & Heintz, T. M. 2021, MNRAS, 506, 2269
El-Badry, K., Rix, H.-W., & Weisz, D. R. 2018, ApJL, 860, L17
Fabrycky, D., & Tremaine, S. 2007, ApJ, 669, 1298
Fellhauer, M., Lin, D. N. C., Bolte, M., Aarseth, S. J., & Williams, K. A. 2003, ApJL, 595, L53
Gaia Collaboration, Prusti, T., de Bruijne, J. H. J., et al. 2016, A&A, 595, A1
Gentile Fusillo, N. P., Tremblay, P. E., Cukanovaite, E., et al. 2021, MNRAS, 508, 3877
Gentile Fusillo, N. P., Tremblay, P.-E., Gänsicke, B. T., et al. 2019, MNRAS, 482, 4570
Grishin, E., & Perets, H. B. 2022, MNRAS, 512, 4993
Grishin, E., Perets, H. B., & Fragione, G. 2018, MNRAS, 481, 4907
Grishin, E., Perets, H. B., Zenati, Y., & Michaely, E. 2017, MNRAS, 466, 276
Hamers, A., Bar-Or, B., Petrovich, C., & Antonini, F. 2018, ApJ, 865, 2
Hamers, A. S., Glanz, H., & Neunteufel, P. 2022, ApJS, 259, 25
Hamers, A. S., Pols, O. R., Claeys, J. S. W., & Nelemans, G. 2013, MNRAS, 430, 2262
Hamers, A. S., & Thompson, T. A. 2019, ApJ, 882, 24
Hawley, W. P., Athanassiadou, T., & Timmes, F. X. 2012, ApJ, 759, 39
Heintz, T. M., Hermes, J. J., El-Badry, K., et al. 2022, ApJ, 934, 148
Hernandez, M. S., Schreiber, M. R., Parsons, S. G., et al. 2022, MNRAS, 517, 2867
Holberg, J. B., Oswalt, T. D., Sion, E. M., & McCook, G. P. 2016, MNRAS, 462, 2295
Hollands, M. A., Tremblay, P. E., Gänsicke, B. T., Gentile-Fusillo, N. P., & Toonen, S. 2018, MNRAS, 480, 3942
Holmberg, J., & Flynn, C. 2000, MNRAS, 313, 209
Hurley, J. R., Pols, O. R., & Tout, C. A. 2000, MNRAS, 315, 543
Hut, P. 1980, A&A, 92, 167
Inight, K., Gänsicke, B. T., Breedt, E., et al. 2021, MNRAS, 504, 2420
Jiménez-Esteban, F. M., Torres, S., Rebassa-Mansergas, A., et al. 2018, MNRAS, 480, 4505
Kaib, N. A., & Raymond, S. N. 2014, ApJ, 782, 60
Katz, B., & Dong, S. 2012, arXiv:1211.4584
Kiseleva, L. G., Eggleton, P. P., & Mikkola, S. 1998, MNRAS, 300, 292
Knigge, C., Baraffe, I., & Patterson, J. 2011, ApJS, 194, 28
Korol, V., Koop, O., & Rossi, E. M. 2018, ApJL, 866, L20
Korol, V., Rossi, E. M., Groot, P. J., et al. 2017, MNRAS, 470, 1894
Kozai, Y. 1962, AJ, 67, 591
Kroupa, P., Tout, C. A., & Gilmore, G. 1993, MNRAS, 262, 545
Kummer, F., Toonen, S., & de Koter, A. 2023, arXiv:2306.09400
Kuntz, A. 2022, PhRvD, 105, 024017
Kupfer, T., Korol, V., Shah, S., et al. 2018, MNRAS, 480, 302
Li, Z., Chen, X., Chen, H.-L., et al. 2020, ApJ, 893, 2
Lidov, M. L. 1962, P&SS, 9, 719
Lim, H., & Rodriguez, C. L. 2020, PhRvD, 102, 064033
Liu, Z.-W., Röpke, F. K., & Han, Z. 2023, RAA, 23, 082001
Lu, C. X., & Naoz, S. 2019, MNRAS, 484, 1506
Mardling, R. A., & Aarseth, S. J. 2001, MNRAS, 321, 398

Marsh, T. R. 2011, CQGra, 28, 094019
Michaely, E. 2021, MNRAS, 500, 5543
Michaely, E., & Perets, H. B. 2014, ApJ, 794, 122
Michaely, E., & Perets, H. B. 2016, MNRAS, 458, 4188
Michaely, E., & Perets, H. B. 2019, ApJL, 887, L36
Michaely, E., & Perets, H. B. 2020, MNRAS, 498, 4924
Michaely, E., & Shara, M. M. 2021, MNRAS, 502, 4540
Moe, M., & Di Stefano, R. 2017, ApJS, 230, 15
Mushkin, J., & Katz, B. 2020, MNRAS, 498, 665
Naoz, S. 2016, ARA&A, 54, 441
Naoz, S., & Fabrycky, D. C. 2014, ApJ, 793, 137
Naoz, S., Farr, W. M., Lithwick, Y., Rasio, F. A., & Teyssandier, J. 2013a, MNRAS, 431, 2155
Naoz, S., Kocsis, B., Loeb, A., & Yunes, N. 2013b, ApJ, 773, 187
Nelemans, G., Portegies Zwart, S. F., Verbunt, F., & Yungelson, L. R. 2001, A&A, 368, 939
Paczyński, B. 1971, ARA&A, 9, 183
Pala, A. F., Gänsicke, B. T., Townsley, D., et al. 2017, MNRAS, 466, 2855
Parthasarathy, M., Branch, D., Jeffery, D. J., & Baron, E. 2007, NewAR, 51, 524
Perets, H. B., & Kratter, K. M. 2012, ApJ, 760, 99
Petrovich, C., & Muñoz, D. J. 2017, ApJ, 834, 116
Pribulla, T., & Rucinski, S. M. 2006, AJ, 131, 2986
Prodan, S., Murray, N., & Thompson, T. A. 2013, arXiv:1305.2191
Raghavan, D., McAlister, H. A., Henry, T. J., et al. 2010, ApJS, 190, 1
Raskin, C., Timmes, F. X., Scannapieco, E., Diehl, S., & Fryer, C. 2009, MNRAS, 399, L156
Rebassa-Mansergas, A., Solano, E., Jiménez-Esteban, F. M., et al. 2021, MNRAS, 506, 5201
Ren, J. J., Raddi, R., Rebassa-Mansergas, A., et al. 2020, ApJ, 905, 38
Rose, S. C., Naoz, S., & Geller, A. M. 2019, MNRAS, 488, 2480
Rosswog, S., Kasen, D., Guillochon, J., & Ramirez-Ruiz, E. 2009, ApJL, 705, L128
Savedoff, M. P. 1966, AJ, 71, 369
Seto, N. 2022, PhRvL, 128, 041101
Shappee, B. J., & Thompson, T. A. 2013, ApJ, 766, 64
Stegmann, J., Antonini, F., & Moe, M. 2022, MNRAS, 516, 1406
Stephan, A. P., Naoz, S., & Gaudi, B. S. 2018, AJ, 156, 128
Stephan, A. P., Naoz, S., & Gaudi, B. S. 2021, ApJ, 922, 4
Stephan, A. P., Naoz, S., Ghez, A. M., et al. 2016, MNRAS, 460, 3494
Stephan, A. P., Naoz, S., Ghez, A. M., et al. 2019, AAS/Division of Dynamical Astronomy Meeting, 50, 202.02
Stephan, A. P., Naoz, S., & Zuckerman, B. 2017, ApJL, 844, L16
Thompson, T. A. 2011, ApJ, 741, 82
Tokovinin, A. A. 1997, AstL, 23, 727
Toonen, S., Boekholt, T. C. N., & Portegies Zwart, S. 2022, A&A, 661, A61
Toonen, S., Hamers, A., & Portegies Zwart, S. 2016, ComAC, 3, 6
Toonen, S., Hollands, M., Gänsicke, B. T., & Boekholt, T. 2017, A&A, 602, A16
Toonen, S., & Nelemans, G. 2013, A&A, 557, A87
Toonen, S., Perets, H. B., & Hamers, A. S. 2018, A&A, 610, A22
Toonen, S., Portegies Zwart, S., Hamers, A. S., & Bandopadhyay, D. 2020, A&A, 640, A16
Torres, S., Canals, P., Jiménez-Esteban, F. M., Rebassa-Mansergas, A., & Solano, E. 2022, MNRAS, 511, 5462
Torres, S., Rebassa-Mansergas, A., Camisassa, M. E., & Raddi, R. 2021, MNRAS, 502, 1753
Tremblay, P. E., Hollands, M. A., Gentile Fusillo, N. P., et al. 2020, MNRAS, 497, 130
Wang, B., & Han, Z. 2012, NewAR, 56, 122
Wang, H., Stephan, A. P., Naoz, S., Hoang, B.-M., & Breivik, K. 2021, ApJ, 917, 76
Xuan, Z., Naoz, S., & Chen, X. 2023, PhRvD, 107, 043009
Xuan, Z., Peng, P., & Chen, X. 2021, MNRAS, 502, 4199
Zahn, J. P. 1977, A&A, 57, 383
Zhang, E., Naoz, S., & Will, C. M. 2023, ApJ, 952, 103
Zorotovic, M., & Schreiber, M. 2022, MNRAS, 513, 3587
Zorotovic, M., & Schreiber, M. R. 2020, AdSpR, 66, 1080
Zorotovic, M., Schreiber, M. R., García-Berro, E., et al. 2014, A&A, 568, A68